Research Article

Chemical Review and Letters
journal homepage: www.chemrevlett.com
ISSN (online): 2645-4947 (print) 2676-7279

Photocatalytic activity of hydrothermally prepared nanomaterial $ZnMn_2O_4$ and ZnO thin films on degradation of Congo red dye: A comparison study

Morteza Montazerozohori[1,*], Mahboobeh keighobady[2], Mohammad Hossein Habibi[2] and Omid Dadfar[1]

[1]*Department of Chemistry, Yasouj University, Yasouj 7591874831, Iran.*
[2]*Department of Chemistry, University of Isfahan, Isfahan 81746-73441, Iran*

ARTICLE INFO

Article history:
Received 9 April 2025
Received in revised form 17 May 2025
Accepted 20 May 2025
Available online 20 July 2025

Keywords:
Congo Red
Hydrothermal
Photocatalysis
$ZnMn_2O_4$
ZnO

ABSTRACT

This study focuses on innovative water treatment solutions by investigating the photocatalytic degradation of Congo red dye using two advanced nanomaterials, thin films of zinc oxide (ZnO) and zinc manganese oxide ($ZnMn_2O_4$). Both nanomaterials were derived from nitrate precursors at calcination temperatures of 500, 650 and 800 ˚C. Detailed synthesis protocols were meticulously designed to enhance the structural and morphological properties of the photocatalysts, which aims to maximize their photocatalytic efficiency under UV light irradiation. The characterization was carried out using X-ray diffraction (XRD), energy-dispersive X-ray spectroscopy (EDX), fourier-transform infrared spectroscopy (FT/IR), UV-Visible spectroscopy, diffuse reflectance spectra (DRS) and field emission scanning electron microscopy (FE/SEM). The thin films were prepared using the Doctor Blade technique. The particle size of the nanomaterials used in thin-film fabrication was calculated using the Scherrer equation, yielding values between 22 and 32 nm. Optical studies revealed that $ZnMn_2O_4$ possesses a narrower band gap, ranging from 2.47 to 4.06 eV, compared to ZnO's band gap of 3.36 eV. This narrower band gap enhances light absorption and improves charge separation both key factors for effective photocatalysis. Comparative photocatalytic experiments revealed that $ZnMn_2O_4$ exhibits superior performance over ZnO in degrading Congo red dye, achieving higher degradation efficiency (85.3%) and faster reaction kinetics (0.0138 min-1), compared to ZnO's respective values of 70% and 0.0081 min-1. The superior performance of $ZnMn_2O_4$ is attributed to its optimized electronic structure and increased surface area, which results in a smaller particle sizes and more porous morphology. These findings highlight the potential of $ZnMn_2O_4$ nanocomposites as promising candidates for sustainable and efficient water treatment applications.

1. Introduction

Access to clean and safe water stands as a cornerstone for human survival, economic development, and the health of natural ecosystems [1], making water purification an imperative global challenge [2, 3]. In today's rapidly industrializing world, the surge in industrial waste, agricultural runoff and urban effluents has severely compromised water quality, intensifying the need for innovative treatment methods [4-6]. Among the myriads of contaminants affecting aquatic environments, synthetic dyes such as Congo red are particularly concerning due to their persistent nature, complex molecular structure, and resistance to biodegradation [7-9]. Congo red, extensively used in various industries including textiles, printing, and leather processing, not only imparts vivid coloration to products but also introduces toxic compounds into water bodies that can disrupt aquatic life and pose serious health risks to humans. The urgent need to remove such hazardous dyes from wastewater is underscored by their potential to accumulate in the environment, bioaccumulate through the food chain, and even contribute to the development of antibiotic-resistant bacteria [7, 10-12]. Thus, advancing water treatment strategies to effectively eliminate pollutants like Congo red is critical for ensuring sustainable water supplies, protecting public health, and preserving ecological balance [13-15]. Over the past few

* Corresponding author; e-mail: mmzohory@yahoo.com
https://doi.org/10.22034/crl.2025.515948.1575

decades, numerous treatment methodologies have been explored to tackle the challenge of dye-contaminated wastewater, each with its unique set of advantages and limitations [16, 17]. Conventional techniques, such as adsorption, membrane filtration, and coagulation-flocculation, have been widely adopted due to their relative simplicity and low initial cost; however, these methods often fail to achieve complete degradation of dye molecules and can generate secondary pollutants that complicate the treatment process [16, 18-21].

Advanced oxidation processes (AOPs) represent a pivotal innovation in environmental remediation, particularly in the degradation of persistent organic pollutants. Among these methods, photocatalytic degradation has gained considerable attention due to its efficiency and sustainability. This process utilizes semiconductor materials, such as titanium dioxide (TiO_2), which are activated by light energy to generate reactive oxygen species (ROS), including hydroxyl radicals (•OH) and superoxide anions (O_2^-•). These highly reactive species initiate oxidative reactions that decompose complex organic contaminants, such as synthetic dyes, into benign end products like carbon dioxide (CO_2) and water (H_2O). The effectiveness of photocatalysis depends on various factors, including the wavelength of incident light, the properties of the photocatalyst, and environmental conditions, making it a subject of extensive research for optimizing pollutant removal in water treatment applications [22-29]. This process offers a dual advantage by not only decomposing the pollutants but also mitigating the formation of undesirable by-products, thereby presenting a sustainable and efficient alternative for large-scale wastewater treatment applications. The increasing interest in photocatalytic methods is driven by their potential to harness renewable energy sources, such as sunlight, and their applicability in diverse environmental settings, making them a subject of intense research and practical interest [30-35]. Central to the domain of photocatalytic water treatment is the formulation and optimization of resilient, high-performance photocatalysts, with nanostructured materials assuming a critical and transformative role in driving recent technological advancements [36-38]. Zinc oxide (ZnO) nanoparticles have attracted widespread attention owing to their remarkable UV light absorption, high photocatalytic activity, and large surface-to-volume ratio, which facilitates enhanced interaction with pollutant molecules [39-42]. Moreover, tailoring these nanoparticles by incorporating transition metal ions can further augment their photocatalytic performance by modifying electronic properties and reducing charge recombination rates [43]. One notable example is the synthesis of zinc manganese oxide ($ZnMn_2O_4$) nanoparticles, wherein the incorporation of manganese ions into the ZnO lattice not only narrows the band gap but also introduces defect states that enhance electron–hole separation and increase the generation of reactive oxygen species [44-46]. This strategic modification results in a material with superior catalytic efficiency, better stability, and extended light absorption capabilities compared to its pristine counterpart. The unique properties of these nanomaterials, including their tunable band structures, high reactivity, and exceptional surface properties, underscore their potential as next-generation photocatalysts in the degradation of environmentally hazardous dyes [47-50]. The enhanced photocatalytic properties of ZnO and $ZnMn_2O_4$ nanoparticles are particularly significant when applied to the degradation of stubborn pollutants like Congo red [51, 52].

In overall, though nanostructured compounds have been used widely but use of thin films of such nanocompounds may have various advantages. Among many others, the objective of this study is to synthesize $ZnMn_2O_4$ and ZnO nanocompounds via hydrothermal and precipitation methods, respectively, and then detailed comparative analysis of the photocatalytic performance of their thin films on the degradation of Congo red dye. Thin-film materials offer significant advantages in photocatalysis by enhancing surface area, improving charge separation, and allowing precise control over morphology. Their tunable optical properties maximize light absorption, increasing photocatalytic efficiency. Additionally, thin films provide superior stability compared to nanopowders, facilitating easy reuse and integration into industrial applications such as water purification and solar energy conversion. Their scalability and adaptability make them ideal for real-world environmental solutions. In this investigation, an array of advanced analytical techniques, such as X-ray diffraction (XRD), Fourier-transform infrared spectroscopy (FT/IR), UV-Visible spectroscopy, and field emission scanning electron microscopy (FESEM), were utilized to thoroughly characterize the synthesized nanomaterials. The study focused on evaluating their optical, electronic, thermal, bonding, and crystallographic properties, as well as their morphological features and particle size distribution.

2. Materials and methods

2.1. Materials and instruments

Zinc(II) nitrate hexahydrate ($Zn(NO_3)_2{\cdot}6H_2O$)(99.9%), manganese (II) nitrate tetrahydrate ($Mn(NO_3)_2{\cdot}4H_2O$)(98%), ammonia solution(28%), sodium carbonate decahydrate ($Na_2CO_3{\cdot}10H_2O$)(99%), ethanol (C_2H_5OH), double-distilled water, ethyl cellulos(98%), e, terpineol ($C_{10}H_{17}OH$) (96%), polyethylene glycol [$H(OCH_2CH_2)_nOH$] (99%), diethylene glycol $(HOCH_2CH_2)_2O$(99%), acetic acid (CH_3COOH) (99.8%), sodium hydroxide (NaOH) (99%) and were

employed as the starting reagents. Structural analysis was primarily performed using X-ray diffraction (XRD) on a D8 Advance instrument, which operated over a 2θ range from 5° to 80° to determine the crystalline phases present. The crystallite size was determined using the Debye-Scherrer equation:

$$D = 0.9\lambda / (B \cos\theta) \quad \text{Eq. 1}$$

Where D is the crystallite size in nanometers, λ is the wavelength of the Cu Kα radiation (1.5406 Å), B represents the full width at half maximum in radians, and θ is the diffraction angle corresponding to the maximum intensity peak [53, 54]. Complementary to this, thermal properties were examined using a Perkin Elmer STA 6000, providing detailed insights into the stability and decomposition behavior of the materials. Fourier transform infrared spectroscopy (FT/IR) was carried out with a JASCO FT/IR 6300 to elucidate the bonding configurations within the nanocomposites. Optical characterization was conducted using ultraviolet-visible spectroscopy (UV-Vis). Measurements were acquired with both a Varian Cary 500 scan and a JASCO V-670 UV-Vis-NIR spectrometer, covering a wavelength range of 190–900 nm. These analyses allowed for the precise determination of absorption characteristics and the identification of spectral active regions. Diffuse reflection spectra (DRS) were also recorded by JASCO V-670 model instrument to accurately assess the band gap energies of both the semiconductor constituents and their composite forms. Morphological and energy-dispersive X-ray spectroscopy (EDX) investigations were conducted using field emission scanning electron microscopy (FESEM/EDX) on a Cold Emission 4160 Field, Hitachi S model. This technique provided high-resolution images of the nanocomposites, enabling a detailed examination of their surface textures and particle sizes. Thermal processing was performed using a furnace system (model AZAR-FURNACES), ensuring controlled heat treatments during the synthesis process. Dye irradiation experiments were carried out using a 250W high-pressure mercury lamp to evaluate the photocatalytic activity of the nanocompound thin films. A Shimadzu TOC-5050A analyzer was used for TOC measurement.

2.2. Synthesis

2.2.1. Synthesis of zinc oxide nanoparticles

For the synthesis of zinc oxide nanoparticles via the precipitation method using its nitrate precursor, 10 mL of a 0.6 M zinc nitrate hexahydrate solution was prepared. A 0.3 M sodium carbonate decahydrate ($Na_2CO_3 \cdot 10H_2O$) solution was subsequently introduced, effectively regulating the pH of the mixture to 9 by facilitating the controlled dissociation of carbonate species and establishing a stable buffering system. The resulting solution was stirred on a magnetic stirrer at a temperature between 30- 40 °C for 1 hour. After the reaction, the precipitate was filtered and washed with distilled water, then dried in an oven at 60 °C for 2 hours. Finally, the dried precipitate underwent thermal treatment in an electric furnace at 500 °C for 2 hours. Fig.1 outlines the synthesis of zinc oxide nanoparticles using the nitrate precursor.

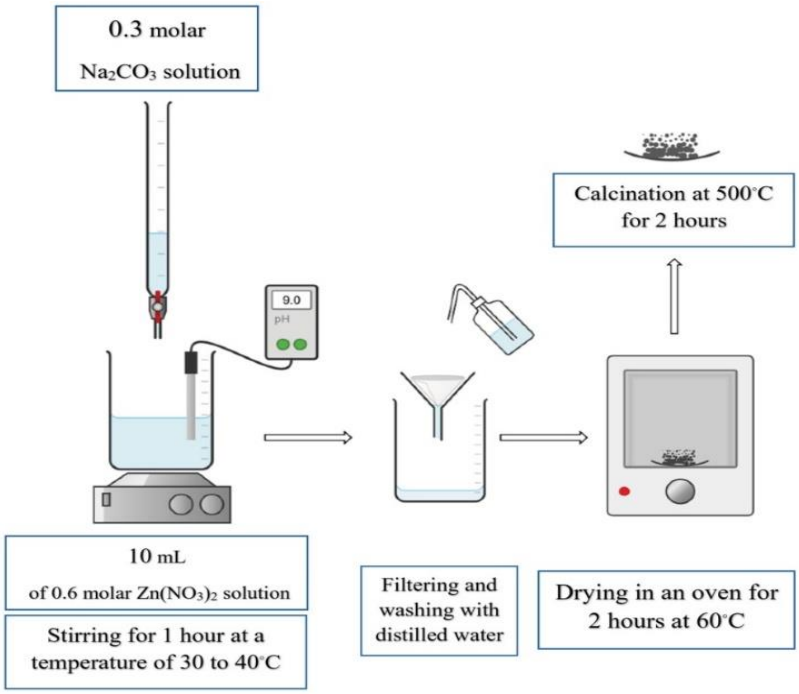

Fig. 1. The general schematic for the synthesis of zinc oxide nanoparticles.

To prepare a zinc manganese oxide nanocomposite by the hydrothermal method, zinc nitrate hexahydrate and manganese (II) nitrate tetrahydrate were employed as the sources of zinc and manganese, respectively, with water

serving as the solvent and ammonia acting as the precipitating agent. Specifically, 1.49 g of zinc nitrate hexahydrate and 2.51 g of manganese (II) nitrate tetrahydrate were dissolved in 40 mL of double-distilled water under magnetic stirring, and 1 mL of polyethylene glycol was added to achieve a clear solution. A 28% ammonia solution was then slowly introduced dropwise until the pH reached 10. The resulting solution was continuously stirred at room temperature for 5 hours using a magnetic stirrer. Following this, the mixture containing the precipitate was transferred to an autoclave and maintained at 160 °C for 24 hours. Once the autoclave cooled to room temperature, the product was extracted, collected via centrifugation, and washed several times with a water-ethanol mixture. The recovered product was dried at 120 °C for 5 hours. Finally, the dried precipitate underwent thermal treatment in an electric furnace at 650 and 800 °C for 2 hours Fig. 2 outlines the hydrothermal synthesis process for the zinc manganese oxide nanocomposite.

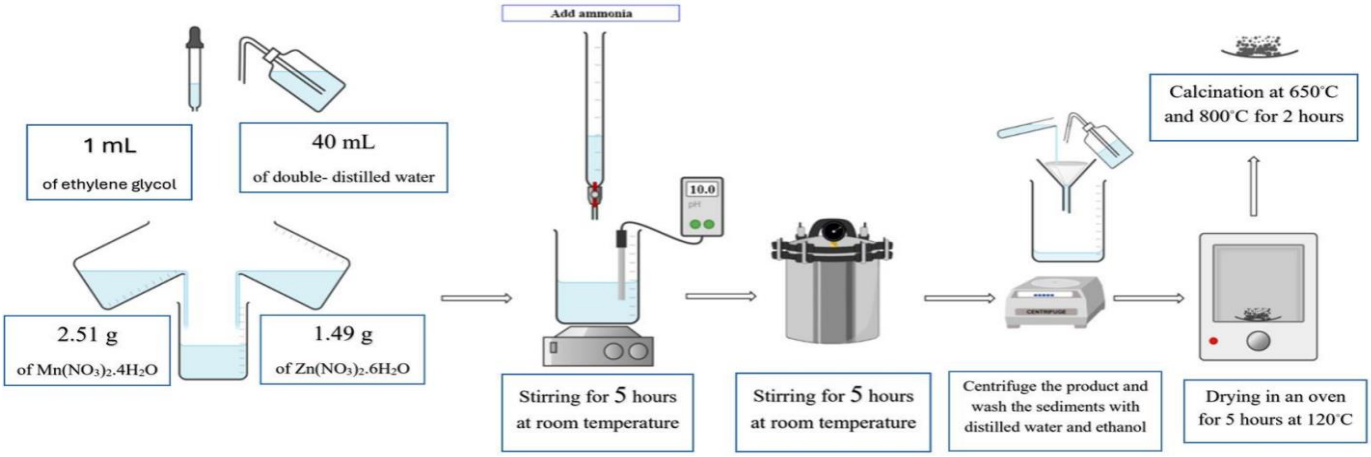

Fig. 2. The general schematic for the synthesis of zinc manganese oxide nanoparticles.

2.2.3. Preparation of paste for thin film production to assess photocatalytic performance

To formulate a stable and homogenous paste incorporating synthesized nanocompounds, a carefully selected combination of ethyl cellulose, terpineol, absolute ethanol, and stearic acid was employed, each playing a distinct role in enhancing the structural and chemical integrity of the dispersion. Ethyl cellulose, a crucial binder, provided mechanical stability and ensured uniform matrix formation. Absolute ethanol acted as both a solvent and a dispersing agent, efficiently dissolving ethyl cellulose while promoting the even distribution of nanoparticles within the medium. Terpineol contributed to the long-term stability of the paste by preventing phase separation, thereby maintaining consistency over extended periods. Furthermore, stearic acid played a role in modifying the surface properties of the nanoparticles, reducing interparticle interactions and improving dispersion quality. To achieve optimal homogeneity and prevent nanoparticle agglomeration, ultrasonic waves were employed, facilitating uniform dispersion and enhancing the functional performance of the final formulation. This systematic approach ensures the paste's structural integrity and enhances its suitability for applications requiring precise nanomaterial distribution. Initially, 8.0 g of nanostructured compounds was placed in a round-bottom flask on a magnetic stirrer, followed by sequential additions of stearic acid (130 µL), double-distilled water (five successive additions of 130 µL each), absolute ethanol (fifteen successive additions of 130 µL each and six successive additions of 330 µL each), all performed at one-minute intervals under continuous stirring. The resulting mixture was transferred to a 25 mL beaker with 13 mL of absolute ethanol, and ultrasonic waves
were applied three times for durations of 30, 60, and 90 seconds. Subsequently, 3 mL of terpineol was added, followed by another round of ultrasonic treatments with the same durations. Next, 4.0 g of ethyl cellulose, previously dissolved in 5 mL of ethanol, was incorporated, and three additional ultrasonic treatments were applied to ensure complete homogenization. Finally, the solvent was allowed to evaporate entirely under continuous stirring at room temperature, yielding a paste with optimized viscosity and suitable rheological properties for further applications.

2.2.4. Preparation of nanocompound thin films by the Doctor Blade technique

For the fabrication of nanocompound thin films using the doctor blade technique, a paste derived from thermally treated composite nanoparticles was prepared. Before deposition, the glass substrate underwent rigorous cleaning with nitric acid, distilled water, and acetone to eliminate contaminants and ensure optimal adhesion. The substrate was then fixed onto a stationary glass surface

using an adhesive, with the thickness of this adhesive layer precisely controlling the final film thickness. To achieve a uniform coating over a designated 1 cm² area, the adhesive was meticulously applied, after which a controlled amount of the prepared paste was dispensed at both the initial point and midpoint of the substrate. The paste was subsequently spread homogenously using a narrow glass cylinder, ensuring consistent film formation. The coated substrate was subjected to thermal treatment in an electric furnace at 550 °C for 2 hours, promoting densification, improved adhesion, and structural integrity. This methodology facilitated the fabrication of nanocomposite thin films incorporating composite nanoparticles synthesized through the hydrothermal technique, which were systematically characterized for their photocatalytic efficiency and functional properties.

2.2.5. Preparation of the Congo red dye solution

To prepare and characterize the dye solution for photocatalytic analysis, a stock solution was first synthesized at a concentration of 10,000 ppm. This primary solution was systematically diluted in successive stages to achieve final concentrations within the range of 5 to 100 ppm. Absorption spectra for solutions of 5, 10, 15, 20, and 25 ppm were recorded using a Cary 500 spectrophotometer, facilitating the precise determination of the dye's maximum absorption wavelength (λmax). A calibration curve was subsequently constructed by plotting absorbance against concentration, and its linear equation served as the analytical tool for quantifying the dye concentration during the assessment of the photocatalytic performance of the nanocompound thin films.

2.3. Photocatalytic Degradation

2.3.1. Photocatalytic degradation using nanocompound thin films

A 10 mg/L dye solution was first prepared and subjected to oxygen gas bubbling for 30 minutes to ensure proper oxygenation. Next, 21 mL of the oxygenated dye solution was transferred into a Petri dish, into which the prepared photocatalyst thin film and a magnetic stir bar were placed. The Petri dish was then kept in the dark on a magnetic stirrer for 1 hour to establish adsorption equilibrium. The initial absorbance of the dye solution was measured using a UV-Vis spectrophotometer. To monitor the progress of the degradation reaction, the Petri dish was exposed to ultraviolet light at predetermined time intervals while stirring continuously. At designated times; the absorption spectrum of the solution was recorded again to track changes in dye concentration.

2.3.2. Influence of ultraviolet light and nanocompound thin films alone on Dye Degradation

To evaluate the photolytic degradation of the dye under ultraviolet irradiation without a photocatalyst, a 10 ppm dye solution was exposed to UV light for the duration of two hours. Absorbance measurements were taken at regular intervals using a UV-Vis spectrophotometer, following the same methodology as the photocatalytic experiments, to quantify the extent of dye decomposition induced by direct UV exposure. In addition to these photolysis tests, control experiments were conducted under dark conditions to investigate the standalone effect of nanocompound thin films in facilitating dye removal, ensuring a comprehensive assessment of both photolytic and adsorption-driven processes.

3. Results and Discussion

This section presents a comprehensive investigation into the structural, morphological, optical, and elemental properties of zinc manganese oxide ($ZnMn_2O_4$) nanocomposites synthesized via the hydrothermal method using nitrate-based precursors. The impact of thermal treatment at various calcination temperatures (500°C, 650°C, and 800°C) is meticulously analyzed to assess phase evolution, crystallinity, particle size distribution, optical behavior, and chemical composition. A suite of advanced characterization techniques, including X-ray diffraction (XRD), Fourier-transform infrared spectroscopy (FT-IR), ultraviolet-visible (UV-Vis) absorption and diffuse reflectance spectroscopy (DRS), Kubelka-Munk analysis, energy-dispersive X-ray spectroscopy (EDX), and field emission scanning electron microscopy (FE-SEM), is employed to provide detailed insights into the material properties. Additionally, the photocatalytic efficacy of $ZnMn_2O_4$ and ZnO thin films is systematically compared to evaluate the influence of manganese incorporation on enhancing photocatalytic activity, offering valuable perspectives for environmental remediation and sustainable energy applications.

3.1 Evaluation of the properties of zinc Oxide Nanoparticles

The X-ray diffraction (XRD) pattern of the zinc oxide (ZnO) nanoparticles synthesized via the precipitation method using zinc nitrate precursor, after 2 hours of thermal treatment at 500 °C, is shown in Figure 3. The positions and relative intensities of the diffraction peaks in the 2θ range from 10° to 80° correspond well with the standard data reported for ZnO with defined lattice parameters. The Bragg reflections of the crystallized zinc oxide nanoparticles in the hexagonal lattice appear at 2θ angles of 31.72°, 34.4°, 36.21°, 47.49°, 56.19°, and 62.8°, corresponding to the (100), (002), (101), (102), (110), and (103) planes, respectively. The diffraction peaks for the (100), (002), and (101) planes are observed with higher intensity, indicating crystal growth in various directions. Additionally, a

preferential growth along the (101) plane was observed at 2θ=36°. The nanoparticle size, after thermal treatment, was calculated based on the maximum peak intensity and its full width at half maximum (FWHM=0.3149) using the Debye-Scherrer formula (Eq. 1) that was found to be 26.01 nm.

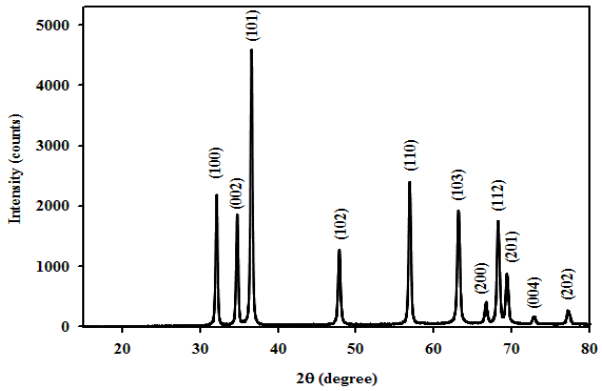

Fig. 3. XRD pattern of ZnO nanoparticles synthesized via the precipitation method using nitrate precursor after 2 hours of thermal treatment at 500 °C.

Figure 4 presents the Fourier Transform Infrared (FTIR) spectrum of zinc oxide (ZnO) nanoparticles synthesized via the precipitation method, utilizing zinc nitrate hexahydrate as the precursor. Following thermal treatment at 500°C, distinct vibrational modes associated with chemical bonding are observed. The peak in region a corresponds to the stretching vibrations of the hydroxyl (O–H) bond, indicative of surface hydroxyl groups or adsorbed water molecules. Additionally, the peak b, detected at approximately 1433 cm^{-1}, is attributed to the stretching vibration of the Zn–O bond, which confirms the formation of ZnO nanoparticles. These spectral features provide critical insights into the structural and chemical properties of the synthesized ZnO, aiding in the evaluation of its purity and functional characteristics [55, 56].

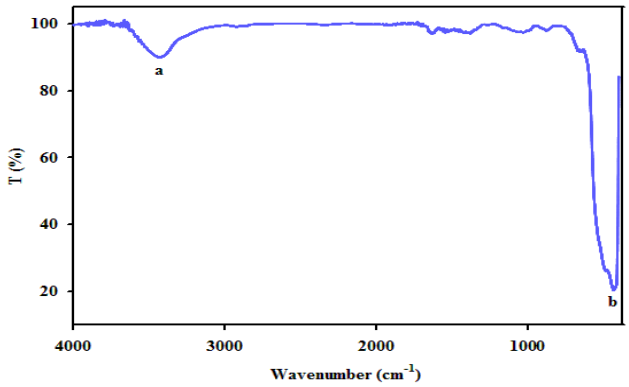

Fig. 4. Fourier Transform Infrared (FT-IR) spectrum of zinc oxide nanoparticles synthesized via precipitation using nitrate precursor after 2 hours of heat Treatment at 500°C.

Figure 5A presents the UV-Visible absorption (UV-Vis-Abs) curve as a function of wavelength for zinc oxide nanoparticles. The optical absorption curve indicates that the sample exhibits an absorption range in the ultraviolet region, specifically within the spectral range of 200–400 nm. The Kubelka-Munk plot of the sample, shown in Figure 5B, was drawn to determine the direct band gap energy of the semiconductor. As illustrated in Figure 5B, the band gap energy was estimated to be 3.36 eV by extrapolating the linear portion of the plot of $[(1-R)^2/(2R)]^2$ versus hν, where R is the reflectance percentage [57, 58].

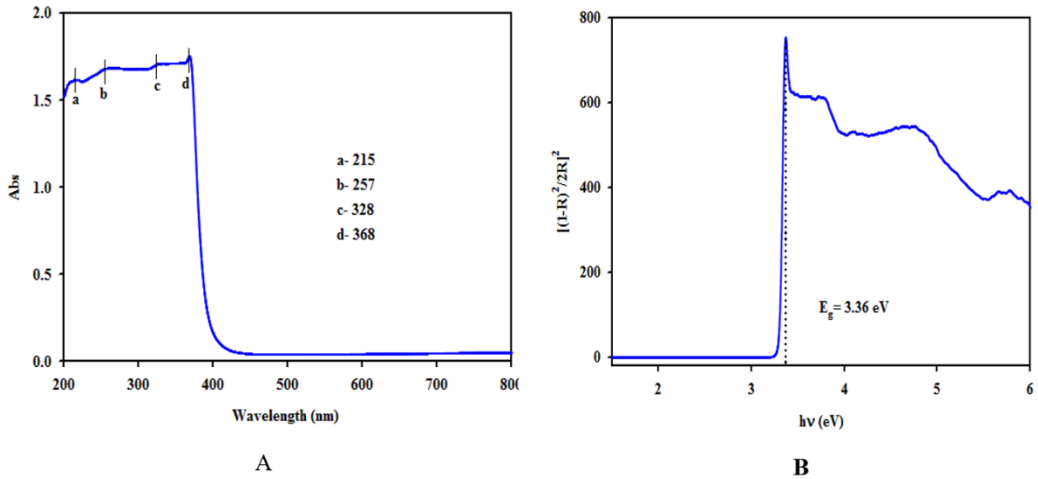

Fig. 5. UV-Visible absorption spectrum(A) and Kubelka-Munk Plot of zinc oxide nanoparticles synthesized via precipitation using nitrate precursor after 2 hours of heat treatment at 500°C.

3.2. Evaluation of the properties of zinc manganese oxide nanocomposite

The zinc manganese oxide nanocomposite synthesized via the hydrothermal method was calcined at 500 °C, 650 °C, and 800 °C for 2 hours, and then analyzed. The X-ray diffraction (XRD) patterns of the zinc manganese oxide nanocomposite obtained at 500 °C, 650 °C, and 800 °C are shown in Figures 6a, 6b, and 6c, respectively. The position and relative intensity of the diffraction peaks in the 2θ range of 10° to 80° for the

sample calcined at 500 °C (Figure 6a) indicate the presence of two phases: ZnO and $ZnMn_2O_4$, which are crystallized in hexagonal and tetragonal systems, respectively. The powders calcined at 650°C (Figure 6b) contain three phases: $ZnMn_2O_4$, ZnO, and Mn2O3, which crystallize in tetragonal, hexagonal, and cubic systems, respectively. Finally, a single-phase crystalline $ZnMn_2O_4$ is formed at the calcination temperature of 800°C, as shown in Figure 6c. The nanoparticle sizes obtained after heat treatments at 500 °C, 650 °C, and 800 °C were estimated based on the peak intensity and full width at half maximum (FWHM) using the Debye-Scherrer equation and are presented in Table 1. As presented in Table 1, the particle sizes of the $ZnMn_2O_4$ nanomaterial are measured as 26.01 nm, 32.02 nm, and 22.04 nm at calcination temperatures of 500 °C, 650 °C, and 800 °C, respectively. The observed trend indicates an initial increase in particle size as the temperature rises from 500 °C to 650 °C, followed by a reduction at 800 °C. This decrease at higher temperatures may be attributed to enhanced phase purity and potential structural rearrangements occurring within the $ZnMn_2O_4$ crystalline framework during thermal treatment.

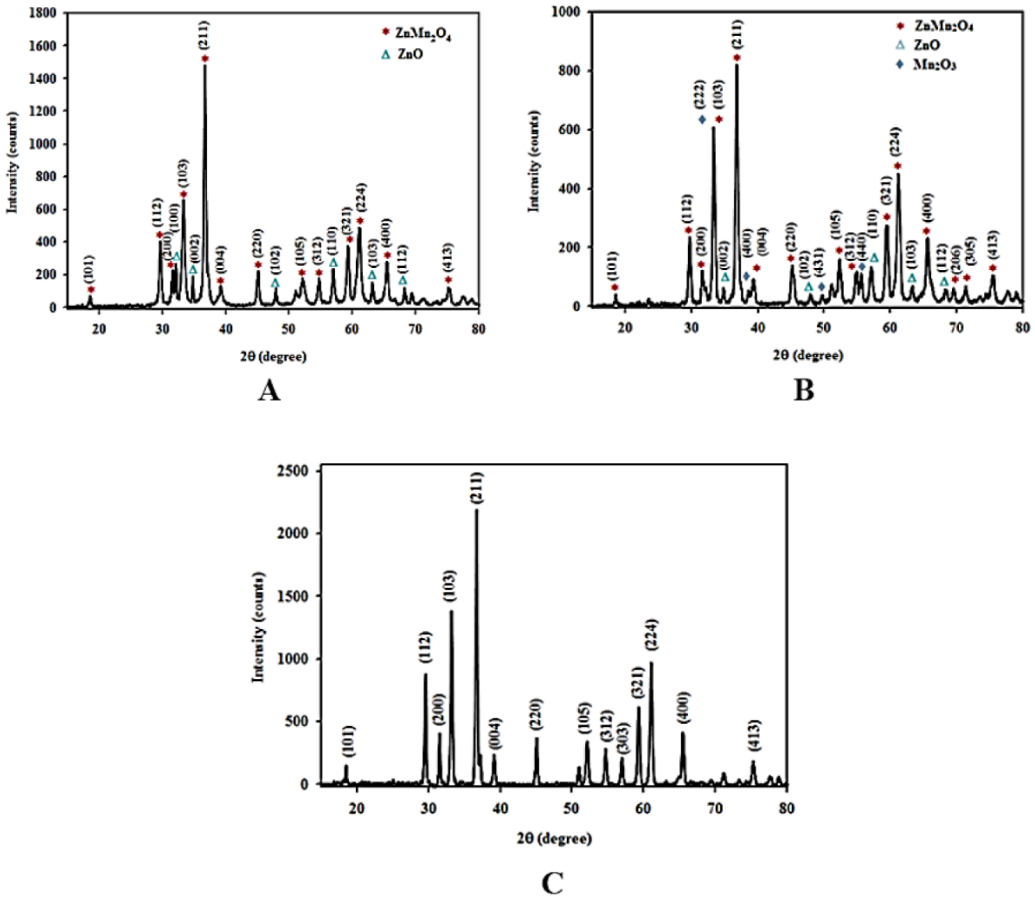

Fig. 6. XRD pattern of zinc manganese oxide nanocomposite synthesized via hydrothermal method using nitrate precursors under 2 hours of heat treatment at A)500 °C, B)650 °C, and C)800 °C.

Figure 7 shows the FT/IR spectra of the powders synthesized via the hydrothermal method using nitrate precursors and subjected to heat treatment at 500°C, 650°C, and 800°C for 2 hours, respectively. In Figure 7, broad peaks observed at 3428 cm^{-1}, 3434 cm^{-1}, and 3429 cm^{-1}, respectively, correspond to the stretching vibrations of water molecules. The peaks at 1642 cm^{-1}, 1642 cm^{-1}, and 1634 cm^{-1} correspond to the bending vibrations of water molecules. This indicates that, in the sample calcined at 800 °C, the intensity of these peaks has decreased due to the evaporation of residual water adsorbed on the surface of the nanoparticles. Two strong, sharp peaks in the 500-800 cm^{-1} range are attributed to the spinel phase.

Table 1. Particle size of zinc manganese oxide synthesized via the hydrothermal method using nitrate precursors after 2 hours of heat treatment at 500°C, 650°C, and 800°C.

Composition	**Calcination Temperature (°C)**	**FWHM(°)**	**Particle Size (nm)**
$ZnMn_2O_4$, ZnO	500	0.3149	26.01
$ZnMn_2O_4$, Mn_2O_3, ZnO	650	0.2558	32.02
$ZnMn_2O_4$	800	0.1574	22.04

Figure 8 shows the UV-Vis absorption curves as a function of wavelength for nanocomposites synthesized via the hydrothermal method using nitrate precursors and calcined at a)500 °C, b) 650 °C, and c) 800 °C. A comparison of the UV-Vis absorption curves indicates that with increasing temperature, a redshift occurs, and absorption in the visible region increases at longer wavelengths.

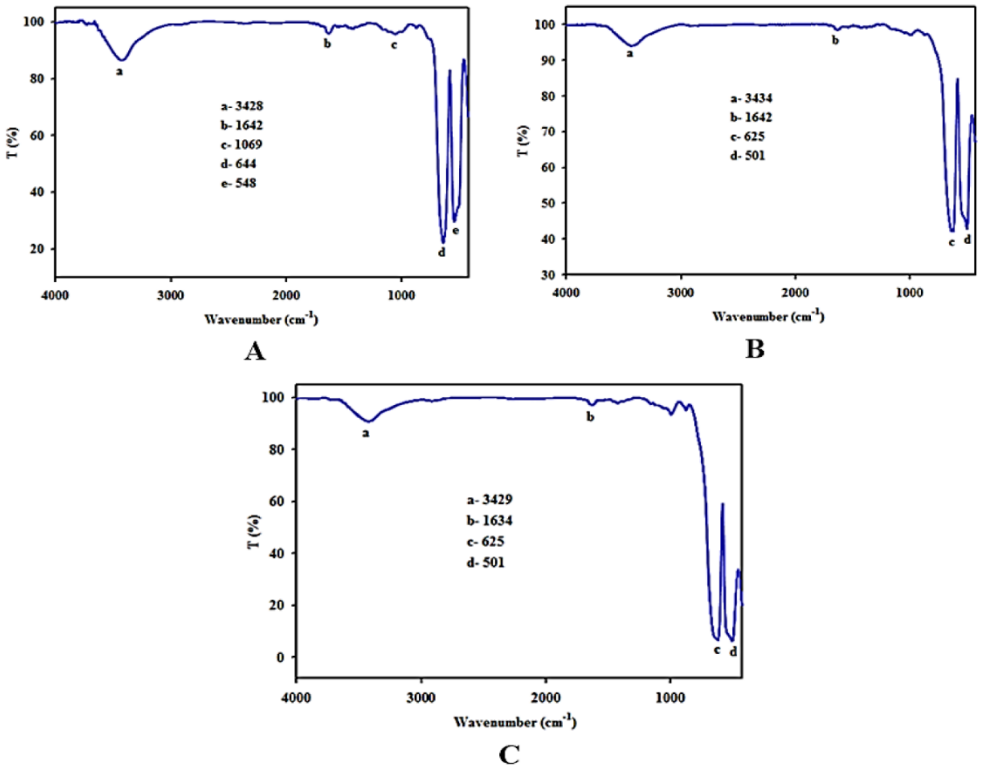

Fig. 7. FT/IR spectra of zinc manganese oxide nanocomposite synthesized via hydrothermal method using nitrate precursors after 2 hours of heat treatment at A)500 °C, B)650 °C, and C)800°C.

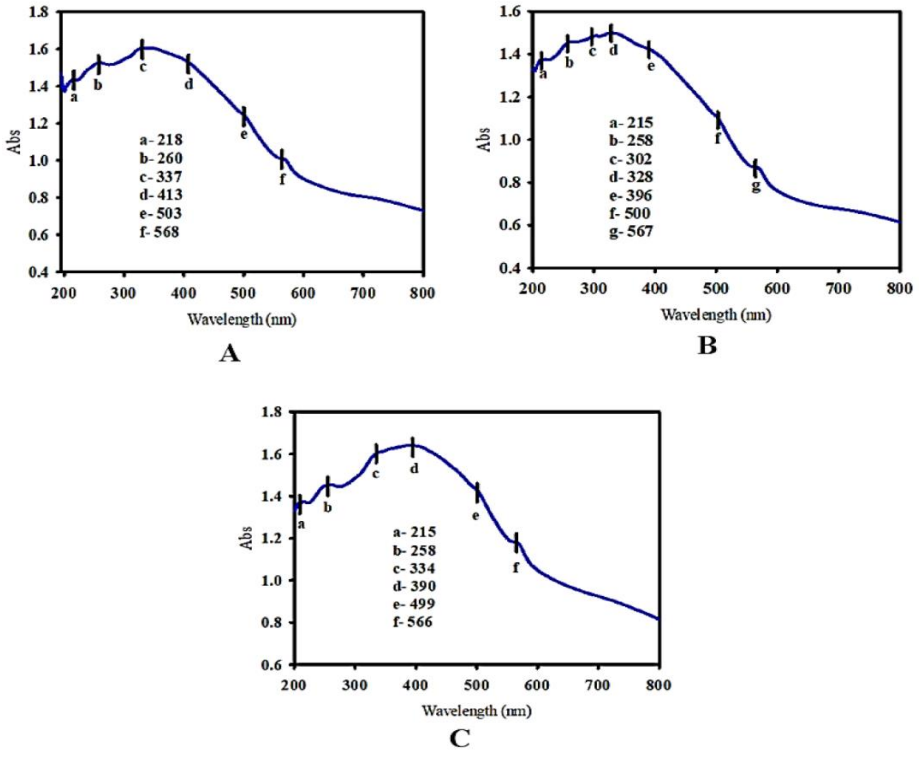

Fig. 8. UV-Vis absorption spectra (UV-Vis-Abs) of zinc manganese oxide nanocomposite synthesized via hydrothermal method after 2 hours of heat treatment at: A) 500°C, B) 650°C, and C) 800°C.

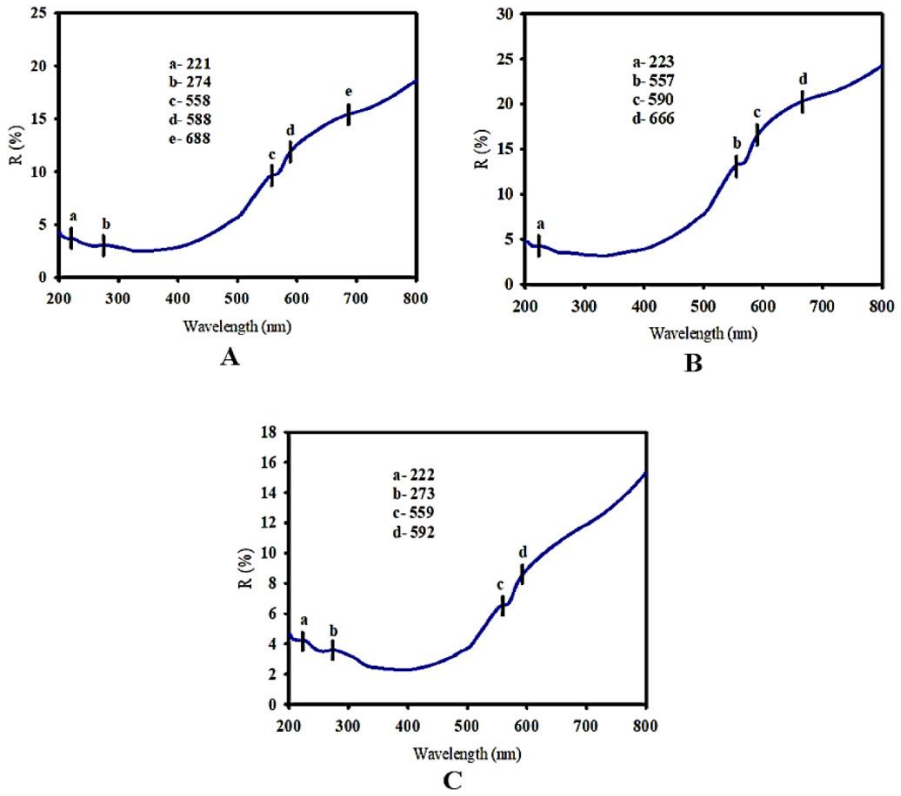

Fig. 9. UV-Vis diffuse reflectance spectra (UV-Vis-DRS) of zinc manganese oxide nanocomposite synthesized via the hydrothermal method after 2 hours of heat treatment at: A) 500°C, B) 650°C, and C) 800°C.

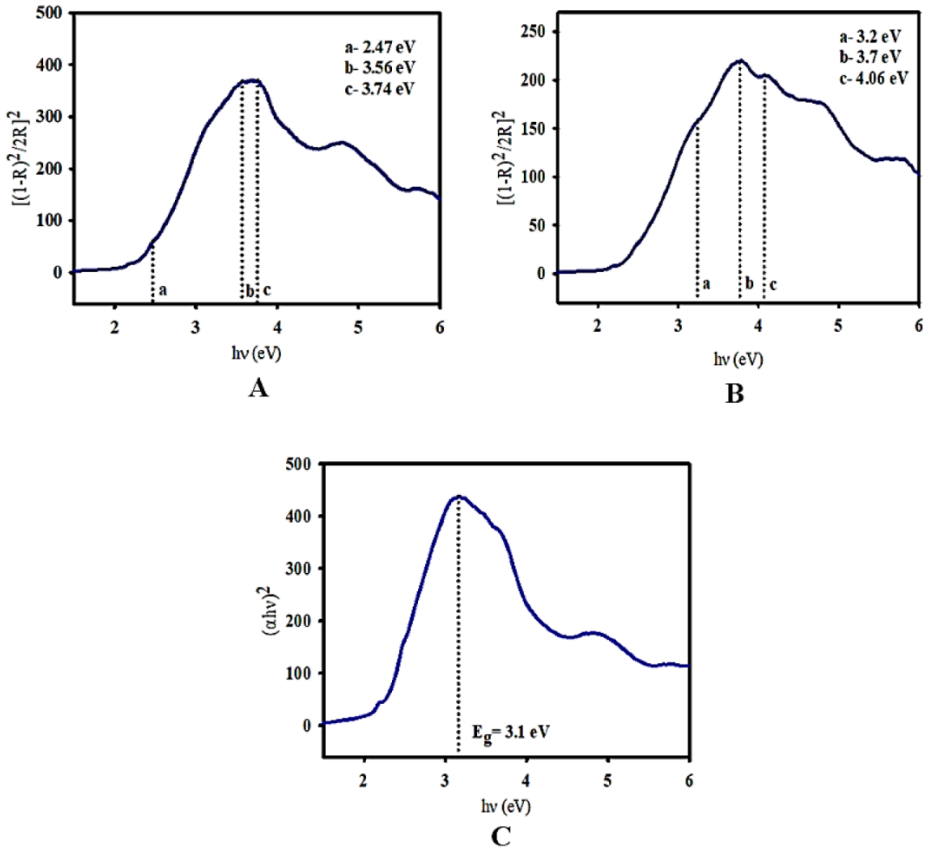

Fig. 10. Kubelka-Munk plots of zinc manganese oxide nanocomposite synthesized via hydrothermal method after 2 hours of heat treatment at: A) 500°C, B) 650°C, and C) 800°C.

Figure 9 shows the UV-Vis diffuse reflectance spectroscopy (UV-Vis-DRS) curves as a function of wavelength for powders synthesized via the hydrothermal method using nitrate precursors and calcined at a) 500 °C, b) 650 °C, and c) 800 °C for 2 hours. The Kubelka-Munk curves for the samples, presented in Figure 10, were plotted to obtain the direct band gap of the semiconductors. The energy band gaps obtained from the UV and visible light absorption for sample a) were 328 nm, b) 337 nm, and c) 390 nm, which correspond to the maximum absorption. The results are summarized in Table 2. Band gap variations in nanomaterials obtained at various calcination temperatures are closely related to phase composition and material purity. Different crystallographic phases exhibit distinct electronic structures, influencing band gap energy and light absorption properties. Additionally, impurities or secondary phases can introduce localized electronic states, altering charge carrier dynamics and photocatalytic efficiency. Higher purity materials typically maintain well-defined band gaps, minimizing unwanted recombination pathways and enhancing performance [59, 60].

Table 2. Band gap energy of zinc manganese oxide nanocomposite synthesized via the hydrothermal method using nitrate precursor.

Calcination Temperature (°C)	Band gap Energy (eV)
500	3.2, 3.7, and 4.06
650	2.47, 3.56, and 3.74
800	3.1

Figure 11 presents the energy-dispersive X-ray spectroscopy (EDX) elemental analysis spectra of zinc manganese oxide ($ZnMn_2O_4$) nanocomposites synthesized via the hydrothermal method using nitrate precursors. The spectra confirm the presence of zinc (Zn), manganese (Mn), and oxygen (O) in the samples, validating the successful incorporation of these elements in the nanocomposite structure. Additionally, Figure 11 displays field emission scanning electron microscopy (FESEM) images of the nanocomposites subjected to a 2-hour thermal treatment at 500°C and 800°C, respectively, providing insight into the morphological evolution of the material as a function of calcination temperature. The average particle sizes were found to be approximately 70 nm and 95 nm. In the sample calcined at 500 °C, the EDX pattern shows the main elements of zinc, manganese, and oxygen in ratios close to the expected composition, and no significant peaks related to impurities or contaminants are observed. Meanwhile, the FESEM images reveal relatively small particles with a moderately porous surface and a more uniform distribution, suggesting that at lower temperatures the particles have fewer tendencies for fusion or excessive growth. In the sample calcined at 800 °C, the EDX peaks for the main elements remain prominent; indicating that the fundamental zinc manganese oxide structure is preserved, although there may be a slight change in the oxygen-to-metal ratio, possibly due to structural alterations at higher temperatures. The FESEM images for this sample show larger, denser particles, some of which are agglomerated, indicating increased sintering and greater crystallite growth at elevated temperatures. Both samples confirm the presence of a similar zinc manganese oxide phase without notable impurities in the reported calcination temperature range, but the key difference lies in the particle size and homogeneity, with the 500 °C sample exhibiting smaller, more porous particles, and the 800 °C sample showing larger, more compact particles, which can ultimately influence physical and chemical properties such as specific surface area and catalytic activity.

3.3. Comparison of the photocatalytic effect of zinc manganese oxide and zinc oxide thin films on the degradation of azo dye Congo red

Figure 12 shows the absorbance versus wavelength plots for the photocatalyst thin film of zinc manganese oxide and zinc oxide. The degradation experiment was carried out over a period of 140 minutes using a Congo red dye concentration of 10 ppm. During this time, the samples were exposed to UV irradiation at specific intervals. The dye solution absorbance was measured using a UV-Vis spectrophotometer, and the degrees of dye degradation as well as the reaction kinetics were investigated. In Figure 12a, corresponding to ZnO, the initial absorption peak (at 0 min) reaches about 0.85 at 500 nm. In contrast, Figure 12 b, representing $ZnMn_2O_4$, shows a slightly lower initial peak of about 0.78 at 500 nm. Over 140 minutes, both catalysts exhibit a reduction in the absorption intensity of Congo red. However, by 60 minutes, ZnO reduces the peak to approximately 0.45, whereas $ZnMn_2O_4$ decreases it more significantly to around 0.30. By the end of 140 minutes, ZnO levels off at about 0.20, while $ZnMn_2O_4$ reaches a lower absorbance of roughly 0.10. These observations indicate that both materials are effective in degrading Congo red, yet $ZnMn_2O_4$ demonstrates higher photocatalytic efficiency under the same conditions. The slight shift in the maximum absorption wavelength of the dye may be attributed to different surface interactions between the dye molecules and each catalyst, while the more pronounced drop in absorption in the $ZnMn_2O_4$ system suggests that manganese incorporation could enhance the catalytic degradation of the dye. Manganese doping enhances photocatalytic performance by modifying crystallinity, porosity, and electronic structure. The introduction of Mn into the lattice induces distortions that influence grain size and phase composition, optimizing charge carrier mobility and reducing recombination rates. Additionally, Mn doping alters surface morphology, increasing porosity and

surface area, which leads to a greater number of active sites for photocatalytic reactions. On an electronic level, Mn creates localized states within the bandgap, shifting optical absorption toward the visible spectrum, thereby improving light harvesting and charge separation efficiency. These combined effects contribute to improved photocatalytic activity, making Mn-doped materials highly effective for applications such as water purification and solar-driven chemical processes [61-63].

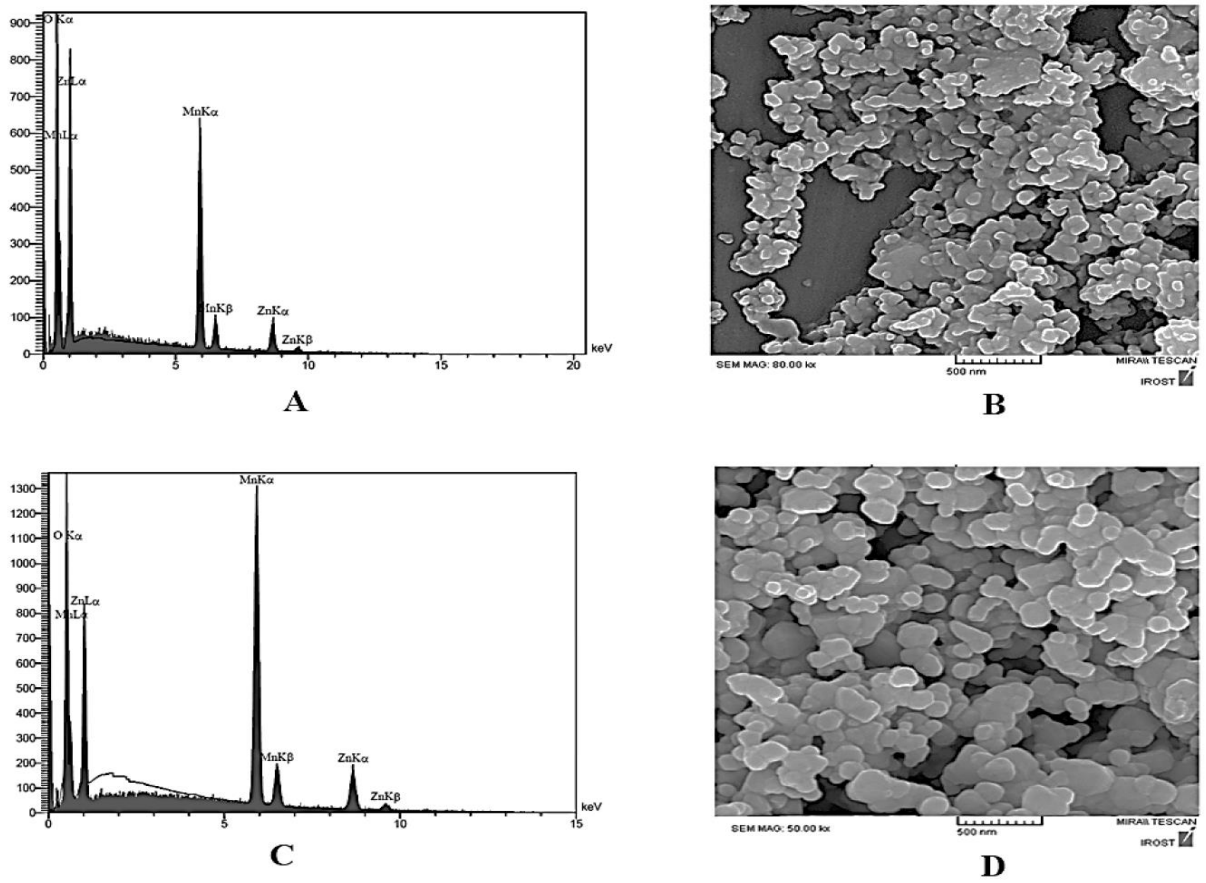

Fig. 11. The EDX pattern and FE/SEM images of zinc manganese oxide nanocomposite synthesized via the hydrothermal method using nitrate precursors and calcined at: A, B) 500°C and C, D)800°C.

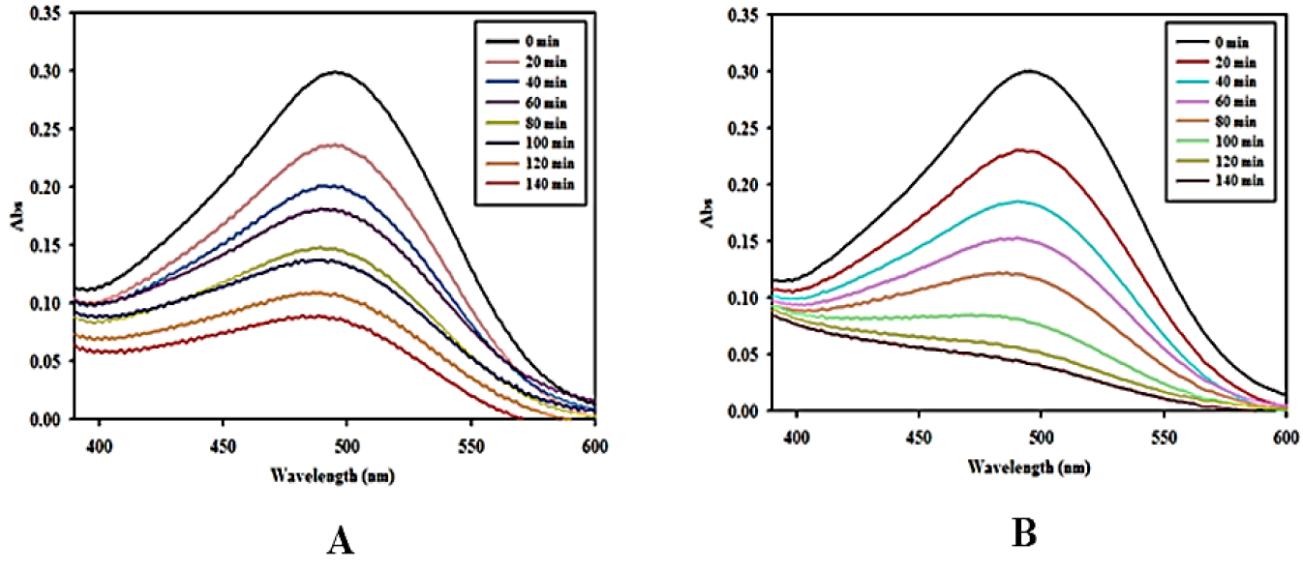

Fig. 12. UV-Vis absorption spectrum of azo dye Congo red with a concentration of 10 ppm over 140 Minutes using Photocatalyst thin film: A) Zinc Oxide and B) Zinc Manganese Oxide.

By comparing the absorbance of each solution with its respective standard curve, the residual dye concentration can be determined, thereby enabling the calculation of photocatalytic degradation efficiency. Figure 13 illustrates the degradation percentage as a function of time for photocatalyst thin films prepared using the Doctor Blade method. These films were employed in the degradation of a 10 ppm Congo red solution (20 mL), providing insight into their effectiveness in dye removal over the treatment period. The graph presents the percentage degradation of Congo red dye over 140 minutes in the presence of thin film photocatalysts: (a) zinc manganese oxide (red line) and (b) zinc oxide (blue line). From the data, it is evident that both photocatalysts facilitate the degradation of Congo red, but zinc manganese oxide ($ZnMn_2O_4$) demonstrates a higher efficiency throughout the irradiation period. At 20 minutes, both catalysts show similar degradation rates, but as time progresses, $ZnMn_2O_4$ consistently achieves greater degradation percentages. At 80 minutes, $ZnMn_2O_4$ reaches approximately 60%, whereas ZnO is around 50%. By 140 minutes, the degradation for $ZnMn_2O_4$ reaches approximately 85%, while ZnO achieves around 70%. The resulting data are summarized in Table 3. The superior performance of the zinc manganese oxide nanocomposite compared to zinc oxide nanoparticles can be attributed to two reasons. First, the size of zinc manganese oxide nanoparticles is smaller than that of zinc oxide nanoparticles, which increases the active surface area and thus enhances the contact between dye molecules and the photocatalyst nanoparticles. Second, the band gap of zinc manganese oxide is smaller than that of zinc oxide, meaning that lower-energy photons are required to generate the electron-hole pairs responsible for driving the photocatalytic activity of the dye.

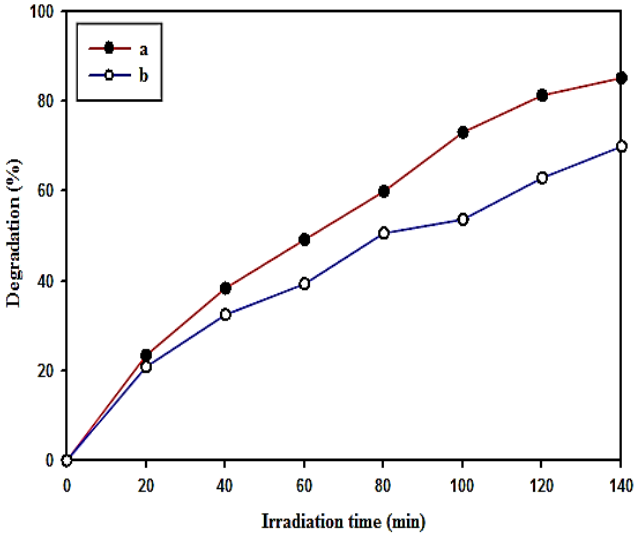

Fig. 13. Percentage degradation of Congo red dye in the presence of photocatalyst thin film (a) zinc manganese oxide and (b) zinc oxide over a period of 140 minutes.The data are the mean of triplicate experiments and rule out photolysis and adsorption portions as major side degradation pathways.

Table 3. Photocatalytic degradation percentage of Congo red dye in the presence of photocatalyst thin films over time, based on spectrophotometric data and the TOC test. The data are the mean of triplicate experiments and rule out photolysis and adsorption portions as major side degradation pathways.

Irradiation time (min)	Zinc manganese oxide thin film	Zinc oxide thin film
20	23.44%	20.86%
40	38.38%	32.48%
60	49.23%	39.36%
80	59.98%	50.67%
100	73.18%	53.75%
120	81.4%	63%
140	85.3%	70%
Degradation based on TOC	85.1%	69%

As a result, electron excitation and transfer from the valence band to the conduction band become simpler. The very slight difference between the spectroscopic data and the Total organic carbon (TOC) test results may be due to instrumental errors or the absorption of environmental CO2 over time before conducting the TOC test.

Numerous studies have explored the degradation of Congo red dye using various nanomaterials and photocatalytic techniques. Although direct comparisons between these reports and the present work are challenging due to differing experimental conditions, several notable findings are highlighted here. Al-Farraj et al. investigated the degradation of a 25 ppm Congo red solution using $MgAl_2O_4$ nanoparticles, achieving an impressive efficiency of 99.27% [64]. In another study, zinc oxide (ZnO) nanoparticles synthesized with Carica papaya leaf extract demonstrated a degradation efficiency exceeding 99% for a 120 ppm dye solution [65]. Additionally, Li et al. reported an 85.36% degradation efficiency using a $Cu_2O/\alpha\text{-}Fe_2O_3$ composite on a 25 ppm dye solution [66]. More recently, a review on Congo red degradation using TiO_2-based photocatalysts under visible light documented efficiencies ranging from 78% to 100% [67]. From this literature analysis, it is evident that while the current photocatalyst thin films exhibit comparable or slightly lower degradation efficiency, their structural and functional advantages including enhanced stability, ease of application, and controlled film thickness offer significant benefits over previously reported materials, reinforcing their potential for practical wastewater treatment applications.

3.4. Comparison of reaction kinetics in the presence of Photocatalyst thin films

To determine the reaction rate constants for degradation, the solution concentrations at different time

intervals were measured using the standard curve. Based on these concentrations, the values of ln(C0/Ct) were calculated, and by plotting ln(Co/Ct) against time as shown in Figure 14, the reaction rate constants were determined. Both curves exhibit an approximately linear trend, indicating pseudo-first-order kinetics. The rate constants for the degradation of Congo red are presented in Table 4. The black circles (Zinc Manganese Oxide) consistently lie above the white circles (Zinc Oxide) throughout the 140 minute experiment, meaning the slope for the Zinc Manganese Oxide photocatalyst is steeper and thus corresponds to a higher apparent rate constant. This difference confirms that doping Zinc Oxide with manganese enhances its photocatalytic performance, likely through improved charge separation or a more favorable electronic structure. Despite their different rates, both materials show a continuous rise in ln(C0/Ct), reflecting ongoing dye degradation and confirming their photocatalytic ability over the entire irradiation period.

Table 4. The reaction rate constants and the percentage of Congo red dye degradation. The data are the mean of triplicate experiments and rule out photolysis and adsorption portions as major side degradation pathways.

Thin Film	Degradation Percentage (%)	k (min^{-1})
Zinc manganese oxide	85.3%	0.0138
Zinc oxide	70%	0.0081

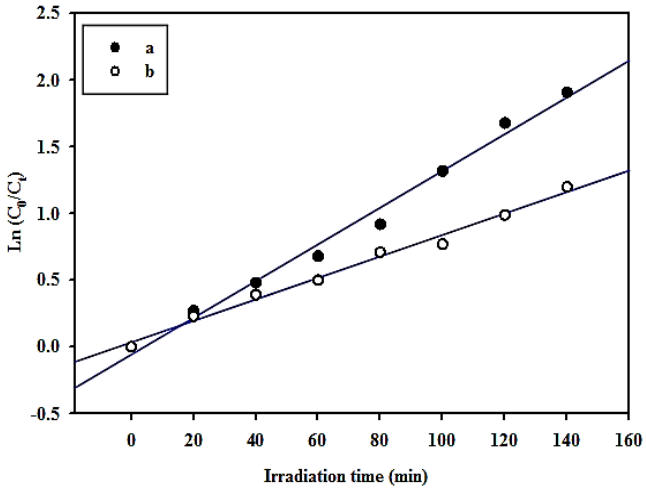

Fig. 14. The graph of **$Ln(C_0/C_t)$** versus time for the photocatalytic degradation reaction of Congo red dye in the presence of photocatalyst thin film: (a) Zinc manganese oxide and (b) Zinc oxide over a period of 140 minutes. The data are the mean of triplicate experiments and rule out photolysis and adsorption portions as major side degradation pathways.

Conclusion

In this study, ZnO and $ZnMn_2O_4$ nanomaterials were synthesized via a calcination method at varying temperatures of 500˚C, 650˚C, and 800˚C, followed by thin film fabrication using the Doctor Blade technique. Structural and morphological analyses, including XRD and FE/SEM, confirm that $ZnMn_2O_4$ synthesized at 800˚C exhibits a distinct crystalline structure and a more favorable particle size distribution (22.04 nm), resulting in a higher active surface area compared to the denser ZnO nanoparticles (26.01 nm). This increased surface area enhances dye adsorption, a critical step in photocatalytic reactions. Furthermore, the narrower band gap of $ZnMn_2O_4$ allows for more efficient utilization of incident light energy, thereby improving its photocatalytic properties. Kinetic studies further substantiate the enhanced performance of $ZnMn_2O_4$, as its higher reaction rate constant—determined through pseudo-first-order kinetics demonstrates accelerated Congo red degradation. Experimental findings affirm the photocatalytic efficacy of both thin film catalysts under UV irradiation, with $ZnMn_2O_4$ exhibiting superior performance, achieving a degradation efficiency of 85.3% and a rate constant of 0.0138 min^{-1}, surpassing ZnO, which recorded 70% efficiency and a rate constant of 0.0081 min^{-1}. The improved photocatalytic activity of $ZnMn_2O_4$ is primarily attributed to manganese incorporation, which effectively modulates the band gap within the range of 2.47–4.06 eV, enhancing charge separation and overall catalytic performance compared to ZnO (band gap: 3.36 eV). Additionally, this enhancement is linked to the catalyst's ability to generate and sustain reactive oxygen species under irradiation, further optimizing its photocatalytic efficiency.

Acknowledgement

Partial support of this work by Isfahan University is acknowledged.

References

[1] S. Singh, R. Jayaram, Attainment of water and sanitation goals: a review and agenda for research, *Sustain. Water Resour. Manag.*, 8(5) (2022) 146.

[2] A. du Plessis, Persistent degradation: global water quality challenges and required actions, *One Earth*, 5(2) (2022) 129-131.

[3] Y. Qi, K. He, Science and Technology for Water Purification: Achievements and Strategies, *Water*, (2025) 91.

[4] D.J. Pandit, A.K. Sharma, Advanced techniques in wastewater treatment: a comprehensive review,Asian J. Environ. Ecol., 23(2024)1-26.

[5] R. Sathya, M.V. Arasu, N.A. Al-Dhabi, P. Vijayaraghavan, S. Ilavenil, T. Rejiniemon, Towards sustainable wastewater treatment by biological methods–A challenges and advantages of recent technologies, *Urban Clim.*, 47 (2023) 101378.

[6] R. Trivedi, T.K. Upadhyay, F. Khan, P. Pandey, R.S. Kaushal, M. Sonkar, D. Kumar, M. Saeed, M.U. Khandaker, T.B. Emran, Innovative strategies to manage

polluted aquatic ecosystem and agri-food waste for circular economy, *Environ. Nanotechnol. Monit. Manag.*, 21 (2024) 100928.

[7] P.O. Oladoye, M.O. Bamigboye, O.D. Ogunbiyi, M.T. Akano, Toxicity and decontamination strategies of Congo red dye, *Groundw. Sustain. Dev.*, 19 (2022) 100844.

[8] K. Sharma, S. Pandit, B.S. Thapa, M. Pant, Biodegradation of Congo red using co-culture anode inoculum in a microbial fuel cell, *Catalysts*, 12(10) (2022) 1219.

[9] A. Tkaczyk, K. Mitrowska, A. Posyniak, Synthetic organic dyes as contaminants of the aquatic environment and their implications for ecosystems: a review, *Sci. Total Environ.*, 717 (2020) 137222.

[10] R. Al-Tohamy, S.S. Ali, F. Li, K.M. Okasha, Y.A.-G. Mahmoud, T. Elsamahy, H. Jiao, Y. Fu, J. Sun, A critical review on the treatment of dye-containing wastewater: ecotoxicological and health concerns of textile dyes and possible remediation approaches for environmental safety, *Ecotoxicol. Environ. Saf.*, 231 (2022) 113160.

[11] N. Tara, S.I. Siddiqui, G. Rathi, S.A. Chaudhry, Inamuddin, A.M. Asiri, Nano-engineered adsorbent for the removal of dyes from water: a review, *Curr. Anal. Chem.*, 16(1) (2020) 14-40.

[12] V. Yadav, D. Tiwari, M. Bhagat, Removal of Congo red dye from aqueous solution by using Limonia acidissima shell as adsorbent, *Asian J. Chem.*, 30 (2018) 2765-2770.

[13] H.W. Ahmad, H.A. Bibi, M. Chandrasekaran, S. Ahmad, G.L. Kyriakopoulos, Sustainable wastewater treatment strategies in effective abatement of emerging pollutants, *Water*, 16(20) (2024) 2893.

[14] A.-A. Mohammed, H. Karaghool, Sustainable adsorption of Congo red dye using organic waste materials as green adsorbents: a mini-review, *Al-Rafidain J. Eng. Sci.*, (2024) 78-86.

[15] S. Sowmya, G. Madhu, R. Sankannavar, S. Yerragolla, Adsorption using chitosan and nano zerovalent iron composite material for sustainable water treatment, *Mater. Res. Express*, 8(2) (2021) 024001.

[16] M.D. Khan, A. Singh, M.Z. Khan, S. Tabraiz, J. Sheikh, Current perspectives, recent advancements, and efficiencies of various dye-containing wastewater treatment technologies, *J. Water Process Eng.*, 53 (2023) 103579.

[17] D. Kumar, S.K. Gupta, Sustainable approach for the treatment of dye-containing wastewater–a critical review, *Rev. Chem. Eng.*, 40(6) (2024) 723-763.

[18] N. Lotha T, V. Sorhie, P. Bharali, L. Jamir, Advancement in sustainable wastewater treatment: A multifaceted approach to textile dye removal through physical, biological and chemical techniques, *ChemistrySelect*, 9(11) (2024) e202304093.

[19] Y.A. Neolaka, A.A. Riwu, U.O. Aigbe, K.E. Ukhurebor, R.B. Onyancha, H. Darmokoesoemo, H.S. Kusuma, Potential of activated carbon from various sources as a low-cost adsorbent to remove heavy metals and synthetic dyes, *Results Chem.*, 5 (2023) 100711.

[20] D. Zerrouki, A. Henni, Dye degradation by recent promising composite, *Novel Mater. Dye-Containing Wastewater Treat.*, (2021) 85-101.

[21] M.K. Al-Hussainawy, Z.S. Mehdi, K.K. Jasim, H.A. Alshamsi, H.R. Saud, H.A.K. Kyhoiesh, A single rapid route synthesis of magnetite/chitosan nanocomposite: Competitive study, *Results Chem.*, 4 (2022) 100567.

[22] S. Anisuzzaman, C.G. Joseph, C.K. Pang, N.A. Affandi, S.N. Maruja, V. Vijayan, Current trends in the utilization of photolysis and photocatalysis treatment processes for the remediation of dye wastewater: A short review, *ChemEng.*, 6(4) (2022) 58.

[23] C. Güleryüz, D.M. Hasan, M.A. Awad, A.S. Waheeb, A.U. Hassan, A. Mohyuddin, H.A.K. Kyhoiesh, M.T. Alotaibi, Molecular engineering on tyrian purple natural dye as TiO_2 based fine-tuned photovoltaic dye material: DFT molecular analysis, *J. Mol. Graph. Model.*, 134 (2025) 108894.

[24] N.H. Imran, N.G. Fahad, M.K. Al-Hussainawy, H.R. Saud, H.A.K. Kyhoiesh, Photocatalytic performance of Soot/TiO_2 nanocomposite against toxic dye, *Mater. Chem. Phys.*, 327 (2024) 129888.

[25] A. Iqbal, A. Yusaf, M. Usman, T. Hussain Bokhari, A. Mansha, Insight into the degradation of different classes of dyes by advanced oxidation processes; a detailed review, *Int. J. Environ. Anal. Chem.*, 104(17) (2024) 5503-5537.

[26] E.H. Khader, S.A. Muslim, N.M.C. Saady, N.S. Ali, I.K. Salih, T.J. Mohammed, T.M. Albayati, S. Zendehboudi, Recent advances in photocatalytic advanced oxidation processes for organic compound degradation: A review, *Desalination Water Treat.*, (2024) 100384.

[27] H. Liu, C. Wang, G. Wang, Photocatalytic advanced oxidation processes for water treatment: recent advances and perspective, *Chem.–Asian J.*, 15(20) (2020) 3239-3253.

[28] P.K. Pandis, C. Kalogirou, E. Kanellou, C. Vaitsis, M.G. Savvidou, G. Sourkouni, A.A. Zorpas, C. Argirusis, Key points of advanced oxidation processes (AOPs) for wastewater, organic pollutants and pharmaceutical waste treatment: A mini review, *ChemEng.*, 6(1) (2022) 8.

[29] R. A. Thura,, T.Z. Fathallah, R. Sattar, Y.A. Naeem, A.H. Idan, H.A.K. Kyhoiesh, Y.M. Nasr, Enhanced photocatalytic removal of direct yellow 50 by ZnO/MWCNTs nanocomposite under solar light irradiation through response surface methodology (RSM) optimization, *Adv. J. Chem. A, 8(2025) 97–106*.

[30] M.A. Al-Nuaim, A.A. Alwasiti, Z.Y. Shnain, The photocatalytic process in the treatment of polluted water, *Chem. Pap.*, 77(2) (2023) 677-701.

[31] S. Balu, D. Ganapathy, S. Arya, R. Atchudan, A.K. Sundramoorthy, Advanced photocatalytic materials-based degradation of micropollutants and their use in hydrogen production–a review, *RSC Adv.*, 14(20) (2024) 14392-14424.

[32] M.A. Iqbal, S. Akram, B. Lal, S.U. Hassan, R. Ashraf, G. Kezembayeva, M. Mushtaq, N. Chinibayeva, A. Hosseini-Bandegharaei, Advanced photocatalysis as a viable and sustainable wastewater treatment process: a comprehensive review, *Environ. Res.*, (2024) 118947.

[33] S. Mishra, B. Sundaram, A review of the photocatalysis process used for wastewater treatment, *Mater. Today Proc.*, 102(2024)393-409.

[34] M. Pavel, C. Anastasescu, R.-N. State, A. Vasile, F. Papa, I. Balint, Photocatalytic degradation of organic and inorganic pollutants to harmless end products: assessment

of practical application potential for water and air cleaning, *Catalysts*, 13(2) (2023) 380.

[35] J. Zhang, H. Wu, L. Shi, Z. Wu, S. Zhang, S. Wang, H. Sun, Photocatalysis coupling with membrane technology for sustainable and continuous purification of wastewater, *Sep. Purif. Technol.*, 329 (2024) 125225.

[36] S.N. Ahmed, W. Haider, Heterogeneous photocatalysis and its potential applications in water and wastewater treatment: a review, *Nanotechnology*, 29(34) (2018) 342001.

[37] G. Ren, H. Han, Y. Wang, S. Liu, J. Zhao, X. Meng, Z. Li, Recent advances of photocatalytic application in water treatment: a review, *Nanomaterials*, 11(7) (2021) 1804.

[38] M. Sharma, S. Nigam, M. Joshi, Design and synthesis of nanostructured photocatalysts for water remediation, *Green Photocatalytic Semicond.*, (2022) 49-74.

[39] A. Barzinjy, Zinc oxide NPs as solar photo-catalysis for water disinfection, *Eurasian J. Sci. Eng.*, 8(2) (2022)69-82.

[40] F. Abdullah, N.A. Bakar, M.A. Bakar, Current advancements on the fabrication, modification, and industrial application of zinc oxide as photocatalyst in the removal of organic and inorganic contaminants in aquatic systems, *J. Hazard. Mater.*, 424 (2022) 127416.

[41] N. Bhattacharjee, I. Som, R. Saha, S. Mondal, A critical review on novel eco-friendly green approach to synthesize zinc oxide nanoparticles for photocatalytic degradation of water pollutants, *Int. J. Environ. Anal. Chem.*, 104(3) (2024) 489-516.

[42] G.K. Weldegebrieal, Synthesis method, antibacterial and photocatalytic activity of ZnO nanoparticles for azo dyes in wastewater treatment: a review, *Inorg. Chem. Commun.*, 120 (2020) 108140.

[43] K. Qi, X. Xing, A. Zada, M. Li, Q. Wang, S.-Y. Liu, H. Lin, G. Wang, Transition metal doped ZnO nanoparticles with enhanced photocatalytic and antibacterial performances: experimental and DFT studies, *Ceram. Int.*, 46(2) (2020) 1494-1502.

[44] K. Lefatshe, G.T. Mola, C.M. Muiva, Reduction of hazardous reactive oxygen species (ROS) production of ZnO through Mn inclusion for possible UV-radiation shielding application, *Heliyon*, 6(6) (2020)e04186.

[45] Y. Liu, Y. Wang, W. Zhen, Y. Wang, S. Zhang, Y. Zhao, S. Song, Z. Wu, H. Zhang, Defect modified zinc oxide with augmenting sonodynamic reactive oxygen species generation, *Biomaterials*, 251 (2020) 120075.

[46] J. Silva, N.A. Neto, M. Oliveira, R. Ribeiro, S. de Lazaro, Y. Gomes, C. Paskocimas, M. Bomio, F. Motta, Recent progress and approaches on the synthesis of Mn-doped zinc oxide nanoparticles: a theoretical and experimental investigation on the photocatalytic performance, *New J. Chem.*, 44(21) (2020) 8805-8812.

[47] M.A. Ahmad, M. Adeel, N. Shakoor, R. Javed, M. Ishfaq, Y. Peng, M. Zain, I. Azeem, I. Ali, M. Usman, Modifying engineered nanomaterials to produce next-generation agents for environmental remediation, *Sci. Total Environ.*, 894 (2023) 164861.

[48] N. Alahmadi, Recent progress in photocatalytic removal of environmental pollution hazards in water using nanostructured materials, *Separations*, 9(10) (2022) 264.

[49] M. Aslam, A.G. Goswami, Bhawna, P. Singh, V. Kumar, B.N. Pant, G. Pandey, K. Kumari, An understanding for the synthesis of metal NPs to photocatalysis to toxicity, *Plasmonics*, 19(6) (2024) 3455-3492.

[50] R.H. Waghchaure, V.A. Adole, B.S. Jagdale, Photocatalytic degradation of methylene blue, rhodamine B, methyl orange, and Eriochrome black T dyes by modified ZnO nanocatalysts: A concise review, *Inorg. Chem. Commun.*, 143 (2022) 109764.

[51] R. Moeinzadeh, N. Azizi, M. Hekmati, M. Qomi, D. Esmaeili, ZnONPs/covalent triazine frameworks nanocomposite as high-performance photocatalysts for degradation of Congo red under visible light, *Mater. Chem. Phys.*, 307 (2023) 128122.

[52] P. Sreelekshmi, R.R. Pillai, S. Unnimaya, A. Anju, A. Meera, Biofabrication of novel ZnO nanoparticles for efficient photodegradation of industrial dyes, *Clean Technol. Environ. Policy*, 26(11) (2024) 3805-3818.

[53] F.T.L. Muniz, M.R. Miranda, C. Morilla dos Santos, J.M. Sasaki, The Scherrer equation and the dynamical theory of X-ray diffraction, *Found. Crystallogr.*, 72(3) (2016) 385-390.

[54] S. Mustapha, M. Ndamitso, A. Abdulkareem, J. Tijani, D. Shuaib, A. Mohammed, A. Sumaila, Comparative study of crystallite size using Williamson-Hall and Debye-Scherrer plots for ZnO nanoparticles, *Adv. Nat. Sci. Nanosci. Nanotechnol.*, 10(4) (2019) 045013.

[55] N.S. Parmar, M.D. McCluskey, K.G. Lynn, Vibrational spectroscopy of Na–H complexes in ZnO, *J. Electron. Mater.*, 42 (2013) 3426-3428.

[56] A. Pieczka, B. Gołębiowska, P. Jeleń, M. Sitarz, A. Szuszkiewicz, Raman spectroscopic studies of O–H stretching vibration in Mn-rich apatites: A structural approach, *Am. Mineral.*, 105(9) (2020) 1385-1391.

[57] J. Bhagwan, J.I. Han, Probing the optical, magnetic, and energy storage properties of co-precipitation routed $ZnMn_2O_4$, *J. Alloys Compd.*, 976 (2024) 173133.

[58] Z.K. Heiba, M. Ghannam, A.M. Abozied, M. Abdellatief, E.E. Ali, A. Badawi, M.B. Mohamed, Investigating the structural, linear/nonlinear optical, and photoluminescence characteristics of $CuO/ZnMn_2O_4$ nanocomposite for physicochemical applications, *ECS J. Solid State Sci. Technol.*, 13(10) (2024) 103011.

[59] R.B. Marcelino, C.C. Amorim, Towards visible-light photocatalysis for environmental applications: band-gap engineering versus photons absorption: a review, *Environ. Sci. Pollut. Res.*, 26 (2019) 4155-4170.

[60] H.L. Tan, F.F. Abdi, Y.H. Ng, Heterogeneous photocatalysts: An overview of classic and modern approaches for optical, electronic, and charge dynamics evaluation, *Chem. Soc. Rev.*, 48(5) (2019) 1255-1271.

[61] N. A. Wahab, N.A. Sairi, Y. Alias, Photocatalytic activities enhancement of manganese-doped ZnO by decoration on CNT for degradation of organic pollutants under solar irradiation, *Appl. Phys. A*, 128(1) (2022) 59.

[62] C. Shyniya, T. Rajasekaran, Investigation on influence of manganese nanoparticles loading in electrochemical activity of anatase titania catalysts and its role in photocatalytic performance, *J. Opt.*, (2022) 1-14.

[63] T. Tsuzuki, Z. Smith, A. Parker, R. He, X. Wang, Photocatalytic activity of manganese-doped ZnO

nanocrystalline powders, *J. Aust. Ceram. Soc.*, 45 (2009)58-62 .

[64] E. S. Al-Farraj, E. A. Abdelrahman, Efficient Photocatalytic Degradation of Congo Red Dye Using Facilely Synthesized and Characterized $MgAl_2O_4$ Nanoparticles. ACS Omega, 9(2024)4870-4880.

[65] J. Gaur, K. Vikrant, K.-H. Kim, S. Kumar, M. Pal, R. Badru, S. Masand, J. Momoh, Photocatalytic degradation of Congo red dye using zinc oxide nanoparticles prepared using Carica papaya leaf extract. Materials Today Sustainability, 22(2023)100339.

[66] Z. Li, X. Chen, M. Wang, X. Zhang, L. Liao, T. Fang, B. Li, Photocatalytic degradation of Congo red by using the Cu2O/α-Fe2O3 composite catalyst. Desalination and Water Treatment, 215(2021)222-231.

[67] G. E. Quintanilla-Villanueva, A. Sicardi-Segade, D. Luna-Moreno, R.E. Núñez-Salas, J.F. Villarreal-Chiu, M. M. Rodríguez-Delgado. Recent Advances in Congo Red Degradation by TiO_2-Based Photocatalysts Under Visible Light. *Catalysts*. 15(2025) 84.